Mechanical Systems and Signal Processing 117 (2019) 210–220

Contents lists available at ScienceDirect

Mechanical Systems and Signal Processing

journal homepage: www.elsevier.com/locate/ymssp

Reverse time migration of acoustic waves for imaging based defects detection for concrete and CFST structures

Hai Liu [a,b], Huiyan Xia [b], Mingwei Zhuang [b], Zhijun Long [b], Chao Liu [a], Jie Cui [a,*], Bin Xu [c,*], Qunfang Hu [d], Qing Huo Liu [e]

[a] School of Civil Engineering, Guangzhou University, Guangzhou 510006, China
[b] Institute of Electromagnetics and Acoustics & Department of Electronic Science, Xiamen University, Xiamen 361005, China
[c] College of Civil Engineering, Huaqiao University, Xiamen 361021, China
[d] Tongji University, Shanghai Institute of Disaster Prevention and Relief, Shanghai 200092, China
[e] Department of Electrical and Computer Engineering, Duke University, NC 27708-0291, USA

ARTICLE INFO

Article history:
Received 16 August 2017
Received in revised form 12 April 2018
Accepted 8 July 2018

Keywords:
Concrete inspection
Non-destructive testing (NDT)
Ultrasonic imaging
Reverse time migration (RTM)
Travel-time tomography

ABSTRACT

Ultrasonic non-destructive testing (NDT) technology has been widely used for defect inspection of concrete structures in civil engineering. However, most of the current data processing methods can only provide qualitative information regarding the existence of concrete inner defects. In this study, an ultrasonic inner defects inspection approach with a high-resolution imaging method which combines travel time tomography (TTT) and reverse time migration (RTM) is proposed for concrete and concrete-filled steel tube (CFST) columns. TTT estimates a reasonable distribution of ultrasonic velocity over the cross-section of the concrete and CFST columns from the first arrival time of the ultrasonic transmission signal. The velocity distribution is used as an input of the initial model for RTM to image the defects inside the concrete and CFST column cross-sections with a high resolution. Numerical experiments demonstrate that the air cavity inside the concrete and CFST columns, and the debonding between the concrete core and the steel tube of the CFST column can be identified clearly, and that the location, size and shape of both defects can be determined accurately. It is concluded that the proposed defect detection approach with a high-resolution imaging method is efficient for the non-destructive inspection of concrete and CFST structures using ultrasonic waves.

1. Introduction

In recent years, concrete-filled steel tube (CFST) columns have been widely employed in high-rise buildings and long-span bridges due to their advanced mechanical behaviors such as higher load-carrying capacity and more ductility under dynamic excitation, compared with normal reinforced concrete (RC) structures. However, various types of defects, such as cracks, air-void, honeycomb and debonding between concrete reinforcement in concrete structures and CFST members impose a huge threat to the structural safety [1]. For example, the interface debonding between concrete core and steel tube of CFST member affects the mechanical behavior of CFST members due to its negative effect on the confinement of steel tube

* Corresponding authors at: School of Civil Engineering, Guangzhou University, Guangzhou 510006, China (J. Cui); College of Civil Engineering, Huaqiao University, Xiamen 361021, China (B. Xu).
E-mail addresses: jcui2009@hotmail.com (J. Cui), binxu@hnu.edu.cn (B. Xu).

https://doi.org/10.1016/j.ymssp.2018.07.011
0888-3270/

on concrete core and finally decrease the load-carrying capacity and ductility. Therefore, the detection for concrete core defect and interface debonding between concrete core and steel tube of CFST is an emergent concern in civil engineering and represents a more challenging task due to the inaccessibility of concrete core covered by steel tube and the electromagnetic shielding effect of steel tube.

Ultrasonic technology has been widely used in nondestructive testing (NDT) and evaluation of concrete structures in civil engineering owing to its high resolution [1,2]. In addition to achievement in ultrasonic testing hardware development, significant progresses have been made in ultrasonic data processing and interpretation for defect detection [4]. Traditional A-scan analysis methods, such as time-frequency analysis [5,6], wavelet analysis [7,8], time-of-flight (TOF) analysis [9] and etc., can be used to analyze signal characteristics and qualitatively detect defects in concrete structures. Xu et al. proposed a piezoceramic lead zirconate titanate (PZT) based active interface debonding detection approach for CFST members and verified the performance of the approach experimentally, but it is still a challenging task to detect the location and dimension of the interface debonding [7,10]. Most of these A-scan data analysis methods can detect the existence of defects in concrete structures but the quantitative evaluation is still a challenging task. From B-scan or C-scan data, ultrasonic imaging techniques can characterize the inaccessible defects embedded in concrete structures.

Tomography utilizing transmission measurements, in which transmitting and receiving transducers are placed on opposite sides of a structure, has been commonly used in seismology and seismic exploration [11–14], and is recently adopted for ultrasonic imaging. Both travel time tomography (TTT) [15] and attenuation tomography [16] have been applied for concrete structure inspection. Experimental application of attenuation tomography to a large concrete structure has been rarely reported. TTT can detect soft defects such as a void, but can hardly detect a hard inclusion such as reinforcement in reinforced concrete structures [17]. Besides, TTT fails to resolve discontinuities in the velocity profile [18] and can only represent the embedded defects as a low-velocity anomaly [15]. Therefore, it is difficult to accurately determine the location and size of concrete defects embedded in concrete structures.

Synthetic aperture focusing technique (SAFT), which is also called migration in seismic data processing, focuses reflected ultrasonic waves recorded at multiple aperture points on one side of a concrete structure and can create a high-resolution image for its defect inspection [3,19,20]. However, SAFT usually utilizes a ray-tracing based back-projection algorithm and cannot handle multiple reflection. Reverse time migration (RTM) is a prestack imaging method based on full wave extrapolation [21] and has been commonly used in seismic exploration in the past twenty years [22]. Although RTM is recognized as the most accurate imaging method among the current migration methods [23], it is sensitive to the initial model, which requires accurate velocity distribution as an input. In practice, the ultrasonic velocity of concrete can be highly variable depending on the aggregate, porosity, temperature and stress. Therefore, it is desired to measure the velocity distribution as an input for RTM to improve the imaging quality.

This paper presents an integrated imaging algorithm, which combines TTT with RTM Specifically, an inhomogeneous velocity distribution over the cross-section of a concrete structure estimated by TTT with a high accuracy is used as the initial velocity model for RTM, of which the imaging quality can be greatly improved. From the reconstructed image by RTM, the defects embedded in both concrete structures and CFST columns are detected and their location and size are accurately determined. The following of this paper is organized as follows. After the introduction to the theory of the proposed imaging algorithm, three numerical experiments on concrete structure with air void and CFST member with air void and interface debonding defects are carried out to validate the advantage of the proposed imaging-based inspection approach. The results and conclusions are given in the fourth and fifth sections, respectively.

2. Proposed integrated imaging algorithm with TTT and RTM

2.1. Acoustic wave equation

Usually, a concrete member such as beam or column or a CFST member can be modeled as a bar or truss member since it extends much longer in one direction than the other two directions. The NDT for a concrete or CFST member is generally carried out with an emphasis on a specific cross-section. It is reasonable to consider a two-dimensional wave equation to describe the acoustic wave propagation in a concrete or a CFST member, where the concrete structure is assumed to be infinitely long in the z direction. Therefore, the first-order velocity-pressure partial differential equation is employed to calculate the acoustic wave fields, as shown in the following equations [24]

$$\begin{cases} \rho \frac{\partial v_x}{\partial t} = \frac{\partial P}{\partial x} + f_x \\ \rho \frac{\partial v_y}{\partial t} = \frac{\partial P}{\partial y} + f_y \\ \frac{\partial P}{\partial t} = \lambda \left(\frac{\partial v_x}{\partial x} + \frac{\partial v_y}{\partial y} \right) + g_p \end{cases} \tag{1}$$

where ρ is the density of the medium, $\boldsymbol{v}_x$, $\boldsymbol{v}_y$ denote the velocity components, P is the pressure, f_x, f_y are the density of a point source, g_p is the density of the pressure source, and λ is the Lame constant. The finite difference time domain (FDTD) method with second-order accuracy in both time and space is employed to solve the first-order differential equation of velocity-pressure [25] and to calculate the wave fields for RTM.

TTT usually uses the method of ray-tracing to calculate the travel time of acoustic transmission signal. However, low velocity zones, which are commonly characterized by the defects in concrete structures, may be represented as shadow zones where rays fail to emerge and the first arrival time may be estimated with a large error [26]. Therefore, a finite difference solution of the Eikonal equation with a scheme of expanding wavefronts is adopted to calculate first arrival time of transmission acoustic waves for TTT in this study [26]. The formula of the Eikonal equation is given by

$$\left(\frac{\partial T}{\partial x}\right)^2 + \left(\frac{\partial T}{\partial y}\right)^2 = s^2(x,y) \tag{2}$$

where $T(x, y)$ is the first arrival time for acoustic energy propagating from a point source through a medium with a slowness (reciprocal of velocity) distribution of $s(x, y)$.

2.2. Rtm

RTM is based on the full wave extrapolation within the cross-section of a concrete member or a CFST member. The flow chart of the RTM imaging algorithm is presented in Fig. 1. It mainly involves three steps [22,27], i.e., forward propagation of the source wave field, back propagation of the recorded receiver data, and imaging condition. Firstly, in the forward propagation (extrapolation), the source wave field is extrapolated from $t = 0$ to t_{max}. Secondly, in the backward propagation (reverse-time extrapolation), backward wave field is generated using the shot data, which represent all the A scans related to the transmitter excitation, recorded by the receiving sensors as the source signal. The receiver wave field is backward extrapolated from $t = t_{max}$ to 0. Then the source wave field and the receiver wave fields are saved. Finally, one RTM image is produced for each source by cross-correlating the source and receiver wave fields at each time using the imaging condition. The imaging condition shows the reflectors where the first arrival of the down-going wave is time coincident with the up-going wave. It is worth noting that these three steps are repeated for all transmitters and the generated RTM images are stacked to produce a final reconstructed image.

The receiver-normalized cross-correlation imaging condition is employed [28], which is given by the following equation,

$$I(x,y) = \sum_n \frac{\sum_t S_n(t,x,y) R_n(t,x,y)}{\sum_t R_n^2(t,x,y)} \tag{3}$$

where $S_n(t,x,y)$ represents the source wave field excited by the n-th transmitter, $R_n(t,x,y)$ represents the receiver wave field that is excited by the signal recorded by the receivers corresponding to the n-th transmitter, which is reversed in time and propagated backward, and $I(x,y)$ is the reconstructed image.

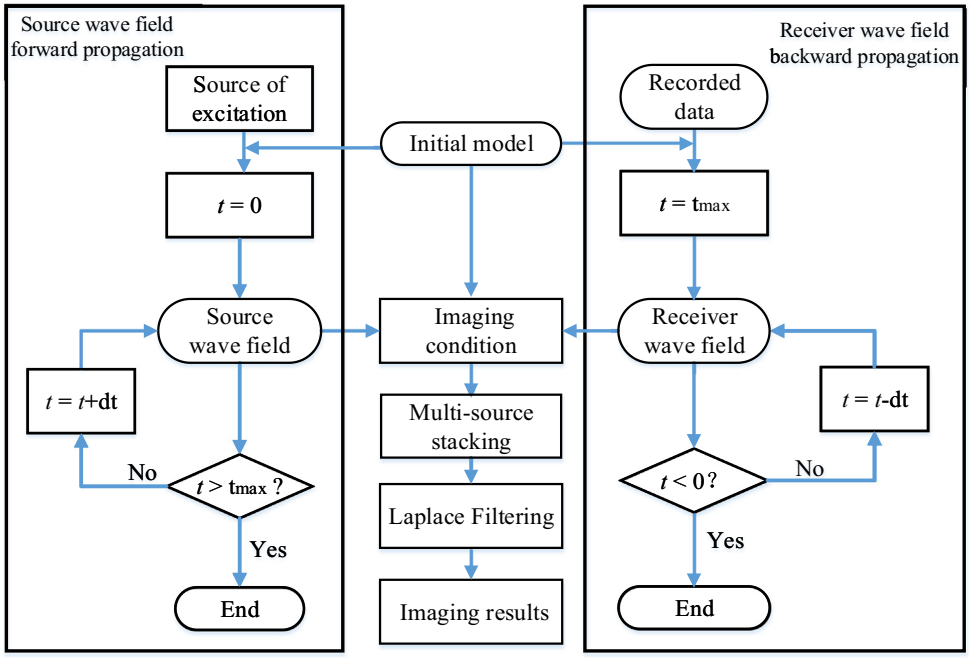

Fig. 1. Flowchart of the RTM algorithm. t_{max} is the time window of the recorded data.

2.3. Ttt

In this study, TTT is employed to estimate a velocity (slowness) distribution across the cross-section of a concrete structure or a CFST member from the first arrival time of the simulated ultrasonic transmission signal, t^{mea}, which is picked from the measured or simulated data by a modified Coppens' method [29]. Firstly, the structural cross-section is discretized and the grids are numbered in a column vector, as illustrated in Fig. 2. The ray path between two grids with different velocity is bent. The computed travel time of the $n-$ th ray from the transmitter to the receiver should be the sum of the travel time of the ray path in each passing grid m, and is given by the following equation [30],

$$\begin{bmatrix} l_{11} & l_{12} & \dots & l_{1m} \\ l_{21} & l_{22} & \dots & l_{2m} \\ \dots & \dots & \dots & \dots \\ l_{n1} & l_{n2} & \dots & l_{nm} \end{bmatrix} \begin{bmatrix} s_1 \\ s_2 \\ \dots \\ s_m \end{bmatrix} = \begin{bmatrix} t_1^{cal} \\ t_2^{cal} \\ \dots \\ t_n^{cal} \end{bmatrix} \tag{4}$$

where t_n^{cal} is the calculated travel time along the n - th path, l_{nm} is the length of the n - th ray in the m - th grid , s_m is the slowness of the m-th grid. Thereby the above equation can be expressed with the following matrix representation $Ls = t^{cal}$. However, due to the limited number of observations, such an ill-conditioned equation has multiple solutions and a least square solution should be found for it, i.e., $\min\| Ls - t^{mea} \|^2$. To solve such an inverse problem, Tikhonov regularization function (objective function) is used to stabilize the solution and it is given by [31],

$$O(s) = \| C_d(Ls - t^{mea}) \|^2 + \alpha^2 \| C_m(s - s^0) \|^2 \tag{5}$$

where C_d is the data weighting matrix in the form of a unit matrix operator, C_m is the model weighting matrix in the form of a Laplace operator, s^0 is the input of initial slowness model, and α is the regularization factor. This inverse problem has to be solved in an iterative way and the above equation can be rewritten as [31],

$$\begin{bmatrix} C_d L^k \\ \alpha C_m \end{bmatrix} (s^{k+1} - s^k) = \begin{bmatrix} C_d(L^k s^k - t^{mea}) \\ 0 \end{bmatrix} (k = 0, 1, 2, 3\dots) \tag{6}$$

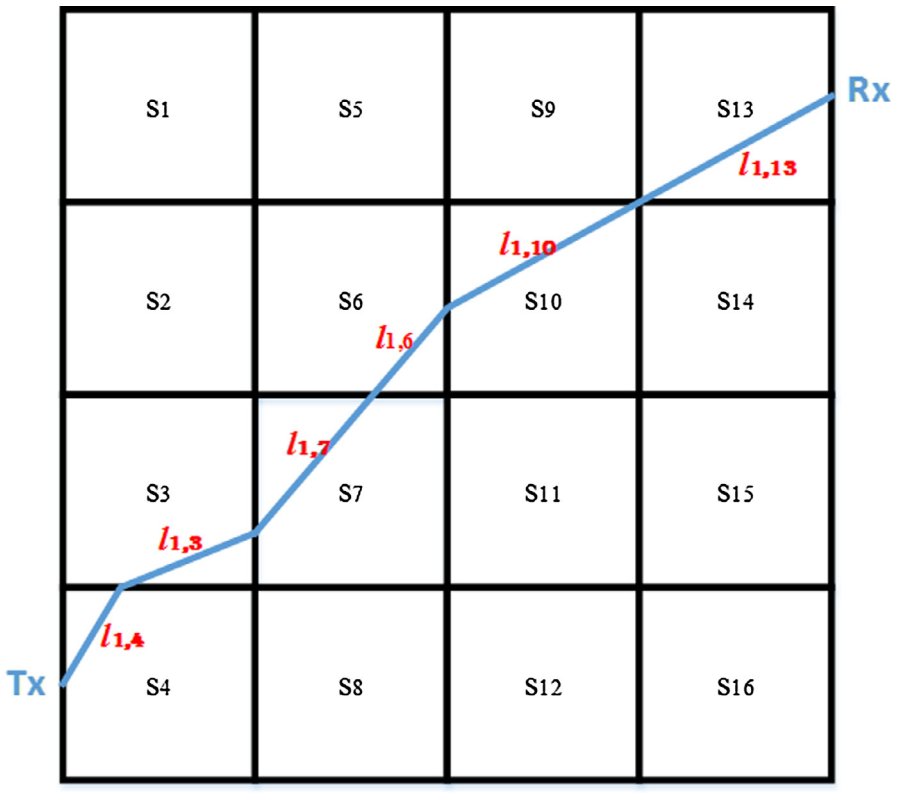

Fig. 2. Sketch of a single ray (taking the first ray as an example) travelling through discretized grids. **Tx** and **Rx** represent the acoustic transmitter and receiver, respectively.

where L^k and s^k are the updated coefficient (Jacobi) matrix and the model vector after the k-th iteration.

The algorithm of TTT is presented in details in Fig. 3. Firstly, an initial slowness model s^0 is used as an input. Next, small perturbation to the slowness model is added to calculate the coefficient matrix L^0 using a finite element approximation method [32]. Then the first arrival time t^{cal} is calculated from the Eikonal equation and the slowness model is updated using Eq. (6). If the objective function is smaller than a predefined value or the iteration number reaches 20 [31], the iteration is terminated and then the velocity distribution is determined.

2.4. Proposed imaging algorithm

In this study, an acoustic imaging method of RTM combined with TTT for the defect detection of concrete member and CFST member is proposed and the main steps are illustrated in Fig. 4. From the picked first arrival time of the measured or simulated transmission acoustic signal, the velocity distribution of the cross-section is estimated and used as an input of initial velocity model for RTM. Then a reflectivity image is reconstructed from the multi-input multi-output signal using RTM. From the RTM image, an air void defect embedded in a concrete structure or a CFST member and the interface debonding defect can be detected and its location, shape and size are expected to be determined accordingly. A Fortran program is developed for simulating the propagation of stress waves and performing the RTM, while the data processing and TTT algorithm are implemented using Matlab.

3. Numerical experiment models for concrete and CFST

Three numerical experiment models for concrete and CFST members are designed to validate the effectiveness of the proposed imaging algorithm combining RTM with TTT for locating and determining the shape and size of the defects embedded in both concrete structures and CFST members. The three models (1 m × 1 m), i.e., a concrete model with an air void (0.4 m × 0.2 m), a CFST column model with an air void (0.4 m × 0.2 m) and a CFST column model with an interface debonding defect (0.2 m × 0.01 m) between concrete core and steel tube, are depicted in Fig. 5. The thickness of the steel tube is 10 mm. Although concrete is inhomogeneous at meso-scale and is composed of coarse and fine aggregates, mortar and interface transition zones, the effects of the meso-scale structure in concrete on the acoustic waves propagation are negligible, compared with those of air defects [33]. The reason is that the impedance contrast between the aggregate and mortar is much smaller than that between air and concrete. Therefore, concrete is modelled as a homogeneous material.

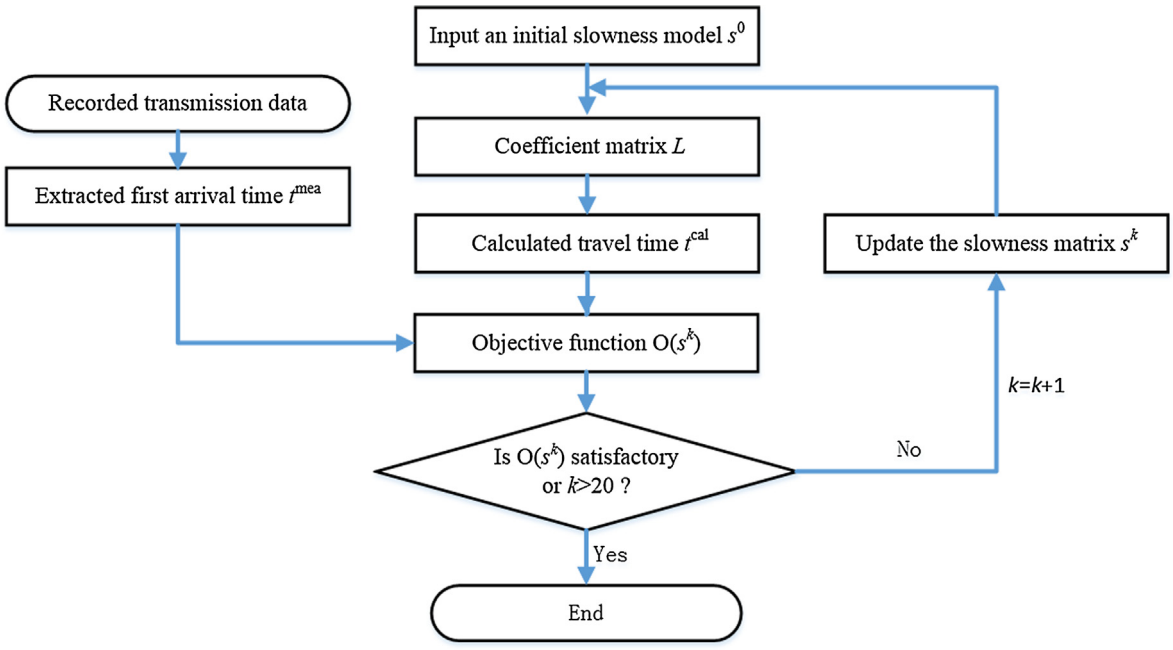

Fig. 3. Flowchart of the TTT algorithm. k is the iteration number.

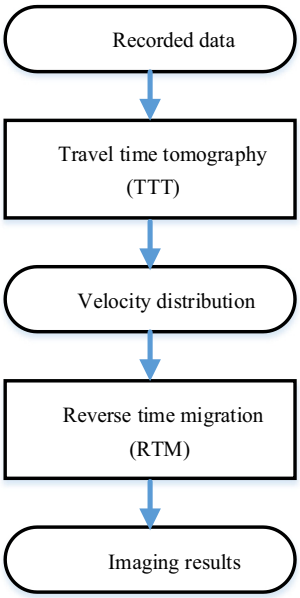

Fig. 4. Flowchart of the proposed acoustic imaging method using RTM in conjunction with TTT.

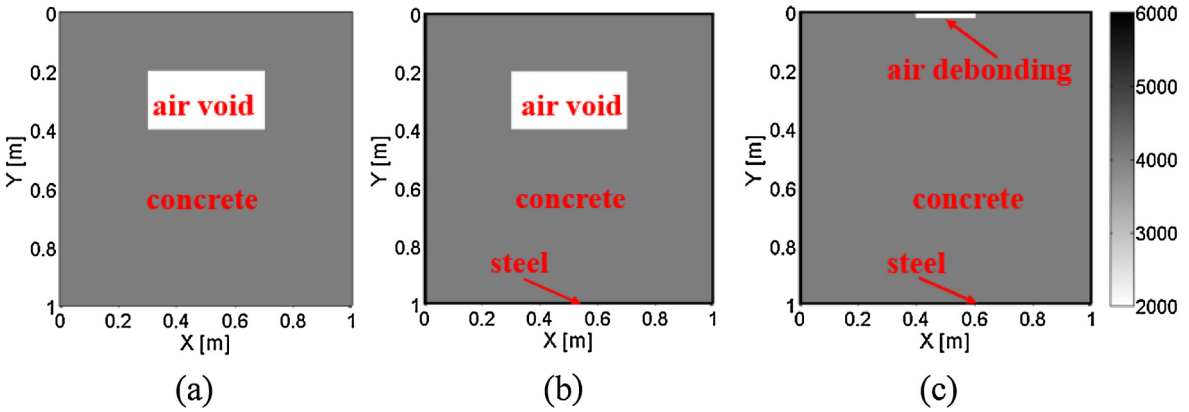

Fig. 5. Numerical experiment models. (a) Concrete model with a 0.4 m × 0.2 m air void, (b) CFST column model with a 0.4 m × 0.2 m air void, and (c) CFST column model with a 10 mm thick and 20 cm long air interface debonding. The thickness of the steel tube surrounding the concrete is 10 mm.

The acoustic velocity in concrete, steel tube and air are set to be 4000 m/s, 5860 m/s and 340 m/s, respectively. The density of concrete, steel tube and air are set to be 2500 kg/m^3, 7850 kg/m^3 and 1 kg/m^3, respectively. A pressure point source [34] is used for wave excitation, and is put on the outer surface of the structures under test in Fig. 5. The directivity of the transducer and impedance mismatch on the air/concrete and steel/concrete interfaces has been modelled by the FDTD simulation. The source waveform used in all the numerical experiments is the first derivative of Blackman-Harris window [35] with a center frequency of 20 kHz as shown in Fig. 6. As shown in Fig. 6(b), the source spectrum has a bandwidth of over 20 kHz, which spans the acoustic band through to the ultrasonic band, and is a good balance between the resolution and penetration for defect inspection of a large concrete structure. Fig. 7 depicts the measurement geometry. Since TTT and RTM make use of the transmission and reflection signal, respectively, their measurement designs are different. In the measurement of TTT, 11 transmitters are placed on the left side of the model and 11 receivers are on the right side. In the measurement of RTM, 44 transceivers are evenly placed on four sides of the model. The spacing between two adjacent transceivers is 20 cm, which is equal to the wavelength of acoustic waves in concrete at the center frequency, i.e. 20 kHz. Outsides the three numerical models with an outer dimension of 1 m × 1 m, an air gap has been added to simulate the actual measurement environment. The FDTD method is used to simulate measurement data [35]. Perfectly matched layers have been used to eliminate the outward acoustic waves to simulate an open boundary [36]. The cross section of each model is discretized by square grids with a size of 2 mm and the time step is set to be 0.228 μs in the FDTD simulations.

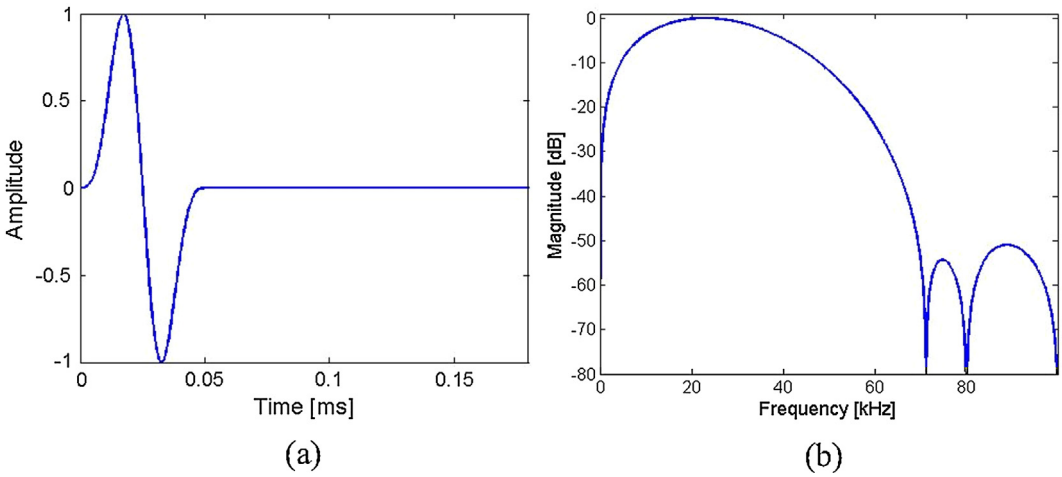

Fig. 6. Blackman-Harris window (BHW) function used for the pressure source in the numerical experiments. (a) Time domain waveform, and (b) frequency spectrum. The center frequency of the BHW wavelet is 20 kHz.

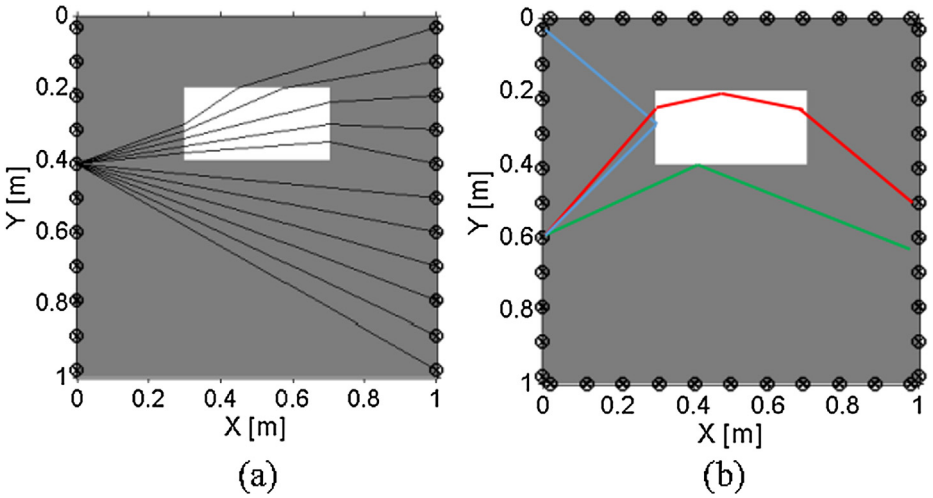

Fig. 7. Measurement geometry for (a) TTT and (b) RTM. The transmitter and receiver are denoted by a circle and a cross, respectively. Typical rays of transmission and reflection signal are respectively drawn in the two figures.

4. Numerical experimental results

The estimated velocity distribution by TTT and the reconstructed image by RTM using the simulated data of the above three numerical models are presented in this section.

4.1. Concrete model with a void defect

Firstly, the influence of velocity distribution of the input model on the RTM imaging results by using the concrete model shown in Fig. 5(a) is investigated. Five homogeneous models as input for RTM, of which the velocity is 3800 m/s, 3900 m/s, 4000 m/s, 4100 m/s and 4200 m/s, respectively, are investigated. The reconstructed images are shown in Fig. 8. When the velocity of the initial model is the same as that of the concrete, i.e., 4000 m/s, the boundary of the air void is satisfactorily imaged with little artifact. The location and size of the air void can be accurately determined. Nevertheless, the image quality is drastically degraded when the velocity deviates from the correct value. When the bias is 5%, i.e., ±200 m/s, the reconstructed images are unacceptable, because the location and size of the air void cannot be accurately determined and other severe artifacts are likely to be interpreted as concrete defects, such as crack. These observations confirm that RTM is sensitive to the initial velocity model. Since the concrete velocity estimated by experience suffers from an unavoidable error, it is desired to estimate a velocity distribution model for RTM.

Then, the results obtained by the proposed imaging algorithm are shown in Fig. 9. Fig. 9(a) shows the estimated velocity distribution from the picked first-arrival time of the simulated transmission signal. It is clear that the velocity of concrete has

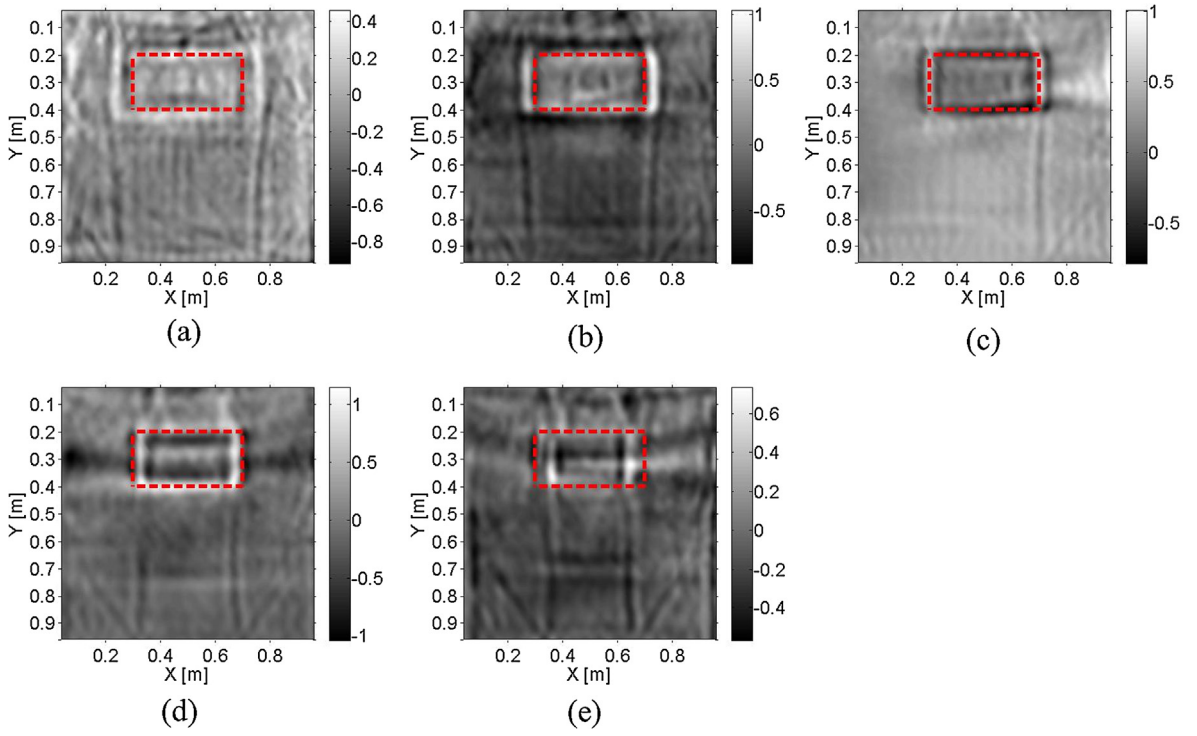

Fig. 8. Reconstructed images of the concrete model in Fig. 5(a) by RTM using homogeneous initial models with a velocity of (a) 3800 m/s, (b) 3900 m/s, (c) 4000 m/s, (d) 4100 m/s, (e) 4200 m/s, respectively. The actual boundary of the air void is marked by a dashed box.

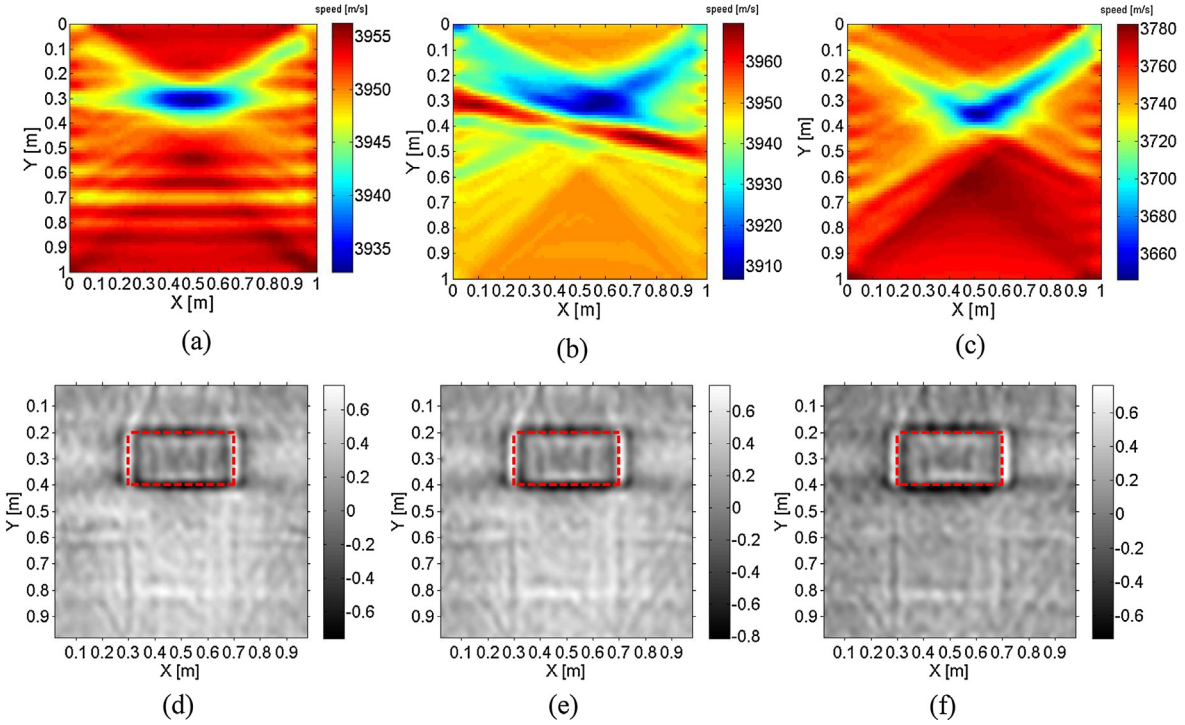

Fig. 9. (a)–(c) Estimated velocity distribution by TTT and (d)-(e) the consequently reconstructed image by RTM using the simulated acoustic data from the concrete model in Fig. 5(a), which is contaminated with no noise, 5% and 10% noise, respectively. The actual boundary of the air void is marked by a dashed box.

been accurately estimated with an error less than about 2%. In contrast, the air void is represented as a blurred low-velocity anomaly, of which the velocity is far from the actually value of 340 m/s. This is because the transmission signal tries to bypass the low-velocity air void (shown in Fig. 7(a)), according to the principle of least time. The shape of the air void is hardly identified in the TTT image. Fig. 9(d) shows the reconstructed image by RTM using the estimated velocity distribution in Fig. 9(a) as an initial model. It can be found that the boundary of the air void is well imaged and its location, shape and size can be determined accurately.

Since noise is unavoidable in a real measurement, the influence of the environmental noise on the imaging results is investigated. The environmental noise in a real measurement set-up for the concrete inspection using acoustic waves has not been experimentally investigated, so we use white Gaussian noise [37]. Here, two levels of white Gaussian noise, 10% and 20%, are added to the simulated data, respectively. The estimated velocity distribution by TTT and the reconstructed images by RTM are shown in Fig. 9(b, e) and (c, f), respectively. The velocity of concrete can still be estimated with a good accuracy in the case of 10% noise. In the case of 20% noise, the concrete velocity is estimated with an error of larger than 5%. In both cases, a low-velocity anomaly has been imaged by TTT in the location of the air void. However, the pattern of the air void is destructively disturbed in the tomographic image due to the influence of noise. In spite of this, the results of RTM seem to be less affected by noise compared with TTT, because little artifacts have been included by comparing Fig. 9(d–f).

4.2. CFST model with a void defect

Different from the concrete model, the CFST model is composed of a concrete core and a steel tube. By the use of the proposed approach, the imaging result using the simulated data from the CFST model (Fig. 7(b)) is shown in Fig. 10. The steel tube is shown as two high-velocity lines on the top and bottom sides of the model, while no response is shown on the left and right sides in the tomographic image, since transmission signal used for tomography is only recorded by sensors set on the top and bottom sides of the structure.

The RTM image for the initial velocity model in Fig. 10(a) is shown in Fig. 10(b). It can be found that the air void is imaged with notable artifacts, compared with the result in Fig. 9(d). In contrast, the steel tube is hardly identifiable in the RTM image. The reason is that the thickness of the steel tube is about 3.4 percent of the wavelength in steel, i.e., 29.3 cm, and such a thin steel tube layer cannot be resolved. Due to the reflection occurs on the steel-concrete interfaces, less acoustic energy impinges on the air void. The RTM image in Fig. 10(b) suffers from more artifacts and the boundary of the air void becomes less focused, compared with that in Fig. 9(d). Nevertheless, the location and size of the air void can be easily identified with an acceptable accuracy.

4.3. CFST column model with an interface debonding defect

Because the thickness of the interface debonding between concrete core and steel tube of CFST member is usually small, its interface debonding detection is challenging. Here, the results of the proposed imaging method using the simulated data from the CFST column model with an interface debonding defect modeled as air (Fig. 5(c)) are shown in Fig. 11. The 10 mm interface debonding is unnoticeable in the tomographic image as shown in Fig. 11(a). Similar to the results in Fig. 10, the steel tube is also unresolvable in the RTM image in Fig. 11(b). Because in practice no defect occurs in steel tube, it is usually

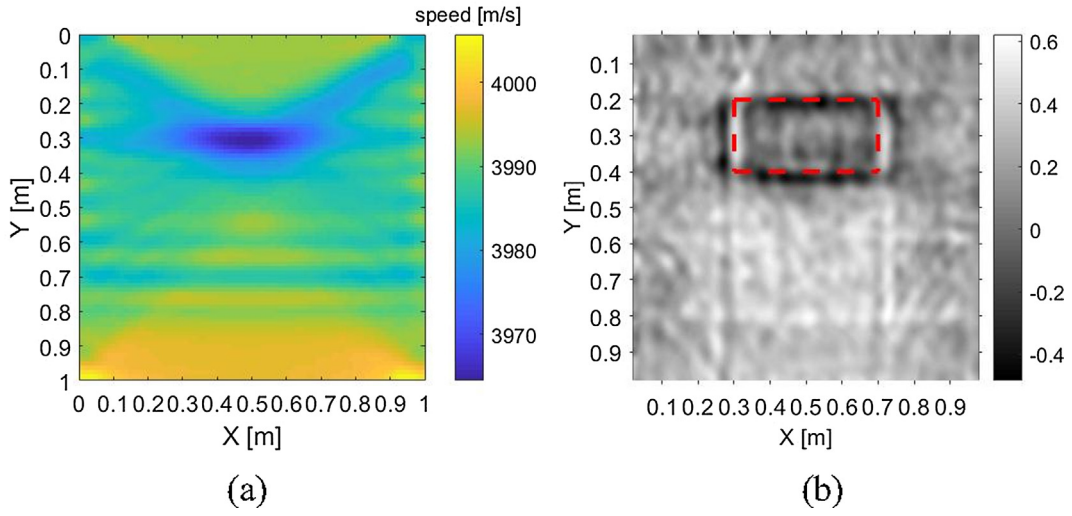

Fig. 10. (a) Estimated velocity distribution from the transmission data simulated from the CFST column model in Fig. 5(b) by TTT and (b) the consequently reconstructed image by RTM. The actual boundary of the air void is marked by a dashed box.

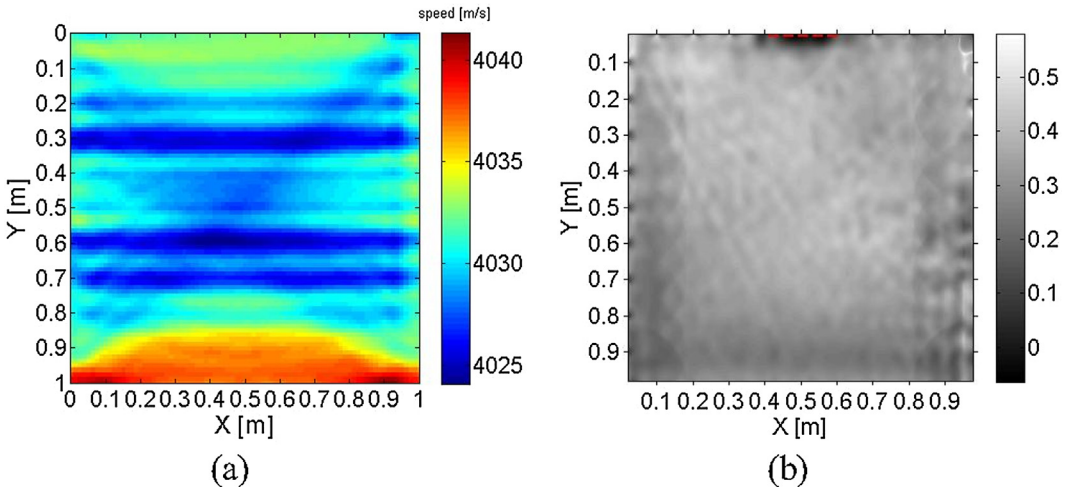

Fig. 11. (a) Estimated velocity distribution from the transmission data simulated from the CFST column model in Fig. 5(c) by TTT and (b) the consequently reconstructed image by RTM. The actual boundary of the air interface debonding is marked by a dashed box.

unnecessary to detect the steel tube. In contrast, the 10 mm air interface debonding defect shows a weak response. This is because 10 mm thickness is larger than half of the acoustic wavelength in air, i.e., 17 mm, and thus the thin air interface debonding is resolvable by RTM.

5. Concluding remarks and future work

In this study, an acoustic imaging method of RTM combined with TTT for the detection of void defects in concrete structure, void in concrete core and the interface debonding defect in CFST members is proposed and numerically validated. By the numerical experiments, the following conclusions can be made.

(1) TTT can only reveal a large defect as a low-velocity anomaly and can hardly determine its shape and size, especially when noise is added. But TTT can provide a reasonable velocity distribution as an initial model for RTM. Compared with the reconstructed image by RTM using a homogeneous velocity model established by experience with an error, that using the TTT-estimated velocity model possesses a higher quality.
(2) Combining TTT with RTM, the existence of a concrete defect embedded inside a concrete structure and a CFST member, and the interface debonding defect between concrete core and steel tube of a CFST member can be easily imaged with a high resolution, even when the air interface debonding in the CFST member is 10 mm in thickness.
(3) The location, shape and size of the air void in a concrete structure and the concrete core and the interface debonding of CFST member can also be accurately determined by the proposed imaging-based defect detection method.

From the current numerical simulation study, it can be found that the proposed acoustic imaging method has great potential for the inspecting of defects in concrete structures and CFST structures and the interface debonding in CFST structures. Future tasks include validation of the approach using laboratory and field experiment measurements using PZT as actuators and sensors. By the use of PZT patches as sensors, it is convenient to excite the structure with a short-pulse ultrasonic source over a desired wide frequency band. Even a large concrete or CFST column is commonly used in high-rise buildings and long-span buildings, it is convenient to attach PZT actuators and sensors on the outside surface of the structure members and the proposed imaging-based inner defects detection approach is applicable.

Acknowledgments

The authors gratefully acknowledge the supports provided by National Key Research and Development Program of China (2016YFC0802400), Guangxi Science and Technology Development Funds (2015BC17047), and National Natural Science Foundation of China (NSFC) under Grant No. 51278185.

References

[1] J. Hola, L. Sadowski, K. Schabowicz, Nondestructive identification of delaminations in concrete floor toppings with acoustic methods, Autom. Constr. 20 (2011) 799–807, https://doi.org/10.1016/j.autcon.2011.02.002.
[2] M. Schickert, Progress in ultrasonic imaging of concrete, Mater. Struct. 38 (2005) 807–815, https://doi.org/10.1617/14298.
[3] G. Trtnik, F. Kavčič, G. Turk, Prediction of concrete strength using ultrasonic pulse velocity and artificial neural networks, Ultrasonics 49 (2009) 53–60.

[4] K. Hoegh, L. Khazanovich, Extended synthetic aperture focusing technique for ultrasonic imaging of concrete, NDT E Int. 74 (2015) 33–42, https://doi.org/10.1016/j.ndteint.2015.05.001.
[5] J.R. Berriman, D.A. Hutchins, A. Neild, T.H. Gan, P. Purnell, The application of time-frequency analysis to the air-coupled ultrasonic testing of concrete, IEEE Trans. Ultrason. Ferroelectr. Freq. Control. 53 (2006) 768–776, https://doi.org/10.1109/TUFFC.2006.1611036.
[6] M.F. Cosmes-Lopez, F. Castellanos, P.F. de J. Cano-Barrita, Ultrasound frequency analysis for identification of aggregates and cement paste in concrete, Ultrasonics 73 (2017) 88–95, https://doi.org/10.1016/j.ultras.2016.08.016.
[7] B. Xu, T. Zhang, G. Song, H. Gu, Active interface debonding detection of a concrete-filled steel tube with piezoelectric technologies using wavelet packet analysis, Mech. Syst. Signal Process. 36 (2013) 7–17, https://doi.org/10.1016/j.ymssp.2011.07.029.
[8] B. Xu, H. Chen, S. Xia, Numerical study on the mechanism of active interfacial debonding detection for rectangular CFSTs based on wavelet packet analysis with piezoceramics, Mech. Syst. Signal Process. 86 (2017) 108–121, https://doi.org/10.1016/j.ymssp.2016.10.002.
[9] M. Luo, W. Li, C. Hei, G. Song, Concrete infill monitoring in concrete-filled FRP tubes using a PZT-based ultrasonic time-of-flight method, Sensors 16 (2016) 2083, https://doi.org/10.3390/s16122083.
[10] B. Xu, B. Li, G. Song, M. Asce, Active debonding detection for large rectangular CFSTs based on wavelet packet energy spectrum with piezoceramics, ASCE J. Struct. Eng. 139 (2013) 1435–1443, https://doi.org/10.1061/(ASCE)ST.1943-541X.0000632.
[11] G. Nolet, Seismic tomography: with applications in global seismology and exploration geophysics, Seism. Encycl. Earth Sci. (1987).
[12] P. Serretti, A. Morelli, Seismic rays and traveltime tomography of strongly heterogeneous mantle structure: application to the Central Mediterranean, Geophys. J. Int. 187 (2011) 1708–1724, https://doi.org/10.1111/j.1365-246X.2011.05242.x.
[13] Z. Wang, D. Zhao, X. Liu, X. Li, Seismic attenuation tomography of the source zone of the 2016 Kumamoto earthquake (M 7.3), J. Geophys. Res. Solid Earth. 122 (2017) 2988–3007, https://doi.org/10.1002/2016JB013704.
[14] J. Chen, C.A. Zelt, P. Jaiswal, Detecting a known near-surface target through application of frequency-dependent traveltime tomography and full-waveform inversion to P- and SH-wave seismic refraction data, Geophysics 82 (2017) R1–R17, https://doi.org/10.1190/geo2016-0085.1.
[15] A. Behnia, H.K. Chai, M. Yorikawa, S. Momoki, M. Terazawa, T. Shiotani, Integrated non-destructive assessment of concrete structures under flexure by acoustic emission and travel time tomography, Constr. Build. Mater. 67 (2014) 202–215, https://doi.org/10.1016/j.conbuildmat.2014.05.011.
[16] H.K. Chai, S. Momoki, Y. Kobayashi, D.G. Aggelis, T. Shiotani, Tomographic reconstruction for concrete using attenuation of ultrasound, NDT E Int. 44 (2011) 206–215, https://doi.org/10.1016/j.ndteint.2010.11.003.
[17] V.G. Haach, F.C. Ramirez, Qualitative assessment of concrete by ultrasound tomography, Constr. Build. Mater. 119 (2016) 61–70, https://doi.org/10.1016/j.conbuildmat.2016.05.056.
[18] R.G. Pratt, N.R. Goulty, Combining wave-equation imaging with traveltime tomography to form high-resolution images from crosshole data, Geophysics 56 (1991) 208–224.
[19] O.V.M. Antonio Jr., S. Hirose, Ultrasonic imaging of concrete by synthetic aperture focusing technique based on hilbert-huang transform of time domain data, Mater. Trans. 53 (2012) 621–626, https://doi.org/10.2320/matertrans.I-M2012804.
[20] M. Schickert, M. Krause, W. Müller, Ultrasonic imaging of concrete elements using reconstruction by synthetic aperture focusing technique, J. Mater. Civ. Eng. 15 (2003) 235–246, https://doi.org/10.1061/(ASCE)0899-1561(2003) 15:3(235).
[21] E. Baysal, D.D. Kosloff, J.W.C. Sherwood, Reverse time migration, Geophysics 48 (1983) 1514–1524.
[22] J. Xie, Z. Guo, H. Liu, Q.H. Liu, Reverse time migration using the pseudospectral time-domain algorithm, J. Comput. Acoust. 24 (2016) 1650005.
[23] J. Zhu, L.R. Lines, Comparing of Kirchhoff and reverse-time migration methods with application to prestack depth imaging of complex structures, Geophysics 63 (1998) 1166–1176.
[24] T. Sakuma, S. Sakamoto, T. Otsuru, Computational Simulation in Architectural and Environmental Acoustics: methods and applications of wave-based computation, Springer, 2014.
[25] Y. Liu, M.K. Sen, Advanced finite-difference methods for seismic modeling, Geohorizons 14 (2009) 5–16.
[26] F. Qin, Y. Luo, K. Olsen, W. Cai, G. Schuster, Finite-difference solution of the eikonal equation along expanding wavefronts, Geophysics. 57 (1992) 478–487.
[27] H. Liu, Z. Long, B. Tian, F. Han, G. Fang, Q.H. Liu, Two-dimensional reverse time migration applied to GPR with A 3D-to-2D, Data Conversion, IEEE J. Sel. Top. Appl. Earth Obs. Remote Sens. 10 (2017) 4313–4320.
[28] S. Chattopadhyay, G.A. McMechan, Imaging conditions for prestack reverse-time migration, Geophysics 73 (2008) S81–S89.
[29] J.I. Sabbione, D. Velis, Automatic first-breaks picking: New strategies and algorithms, Geophysics 75 (2010) V67–V76, https://doi.org/10.1190/1.3463703.
[30] C.A. Zelt, R.B. Smith, Seismic traveltime inversion for 2-D crustal velocity structure, Geophys. J. Int. 108 (1992) 16–34.
[31] F. Wang, S. Liu, X. Qu, Crosshole radar traveltime tomographic inversion using the fast marching method and the iteratively linearized scheme, J. Environ. Eng. Geophys. 19 (2014) 229–237.
[32] D.F. Aldridge, D.W. Oldenburg, Two-dimensional tomographic inversion with finite-difference traveltimes, J. Seism. Explor. 2 (1993) 257–274.
[33] B. Xu, H. Chen, Y.L. Mo, T. Zhou, Dominance of debonding defect of CFST on PZT sensor response considering the meso-scale structure of concrete with multi-scale simulation, Mech. Syst. Signal Process. 107 (2018) 515–528, https://doi.org/10.1016/j.ymssp.2018.01.041.
[34] R. Madariaga, Seismic source: theory, in: G. Schubert (Ed.), Treatise Geophys., Kluwer Academic Publishers, Dordrecht, 2015, pp. 1129–1133, https://doi.org/10.1007/0-387-30752-4_137.
[35] Q.H. Liu, E. Schoen, F. Daube, C. Randall, H. Liu, P. Lee, Three-dimensional finite difference simulation of sonic logging, J. Acoust. Soc. Am. 100 (1996) 72–79.
[36] W.C. Chew, Q.H. Liu, Perfectly matched layers for elastodynamics: a new absorbing boundary condition, J. Comput. Acoust. 4 (1996) 341–359, https://doi.org/10.1142/S0218396X96000118.
[37] J.F. Synnevag, A. Austeng, S. Holm, Adaptive beamforming applied to medical ultrasound imaging, Ultrason. Ferroelectr. Freq. Control. IEEE Trans. 54 (2007) 1606–1613, https://doi.org/10.1109/tuffc.2007.431.